



Nonlinear Acoustic Spin Pumping Caused by Temperature-Dependent Frequency Shifts of Surface Acoustic Waves

Yunyoung Hwang^{1,2} , Jorge Puebla^{2*} , Kouta Kondou² ,
Carlos Sánchez Muñoz³ , and Yoshichika Otani^{1,2†}

¹*Institute for Solid State Physics, University of Tokyo, Kashiwa, Chiba 277-8581, Japan*

²*CEMS, RIKEN, Wako, Saitama 351-0198, Japan*

³*Condensed Matter Physics Center (IFIMAC), Universidad Autonoma de Madrid, Madrid, Spain*

(Received May 11, 2023; accepted July 6, 2023; published online August 3, 2023)

The resonant frequencies of surface acoustic wave (SAW) peaks are known to shift with temperature due to the change in sound velocity of a piezoelectric substrate. Here, we demonstrate that the previously observed nonlinear power dependence of spin current generated by SAWs is a consequence of frequency shifts of SAW peaks due to heating generated at the interdigital transducers. Furthermore, we have observed the emergence of higher-frequency peaks and changes in peak shapes, specifically at high input power. These phenomena are exclusively apparent when utilizing an acoustic cavity constructed with acoustic Bragg reflector gratings. Our systematic study aims at assisting in a deeper understanding of SAW devices in spintronics, particularly, when using acoustic cavities.

1. Introduction

Nonlinear dynamics of mechanical systems have been widely studied,^{1,2)} allowing recent applications of nonlinear physics such as nonlinear optics,³⁾ and 5G and 6G mobile communications systems.⁴⁾ Nonlinear phenomena in surface acoustic waves (SAWs) are mainly caused by nonlinear elastic characteristics of the propagation media and have been well documented since the 1980s.^{5–8)} In our previous research in Ref. 9, we demonstrated the generation of spin currents using SAWs. We employed an acoustic cavity structure, which consists of a pair of Bragg reflector gratings,¹⁰⁾ to confine the SAWs. In this study, we fabricate a sample with a similar structure⁹⁾ to investigate the nonlinear behavior of our spin current generation. We observed a nonlinear behavior of spin current generation dependence with input power. To reveal the origin of this nonlinearity, we measure SAW transmission signals while increasing the input power. We confirm that there are strong frequency shifts of SAWs caused by Joule heat, and show that this nonlinear behavior of SAWs correlates to the nonlinearity of spin current generation as the excitation power increases.

2. Experimental Setup

In order to generate and detect SAWs, we fabricate interdigital transducers (IDT)¹¹⁾ on a LiNbO₃ substrate, which is commonly used as a piezoelectric material for SAW generation. We patterned IDTs and the acoustic cavity by e-beam lithography as shown in Fig. 1(a). We note that, while in our previous research, we fabricated IDTs and acoustic cavities with Ti/Au,⁹⁾ here we fabricate IDTs and reflectors with 35-nm-thick Al deposition, which is known as one of the most common materials for an IDT due to its good balance of low resistivity, low density, and good surface adhesion.¹²⁾ We deposited Al by e-beam evaporation. Between two IDTs, we deposited a Ni/Cu/Bi₂O₃ heterostructure. When SAWs propagate through this heterostructure, magnetization dynamics is excited by magnon–phonon coupling via so-called acoustic ferromagnetic resonance (FMR)^{9,11,13–16)} in the Ni layer. The excited magnetization dynamics pumps spin current into the adjacent Cu

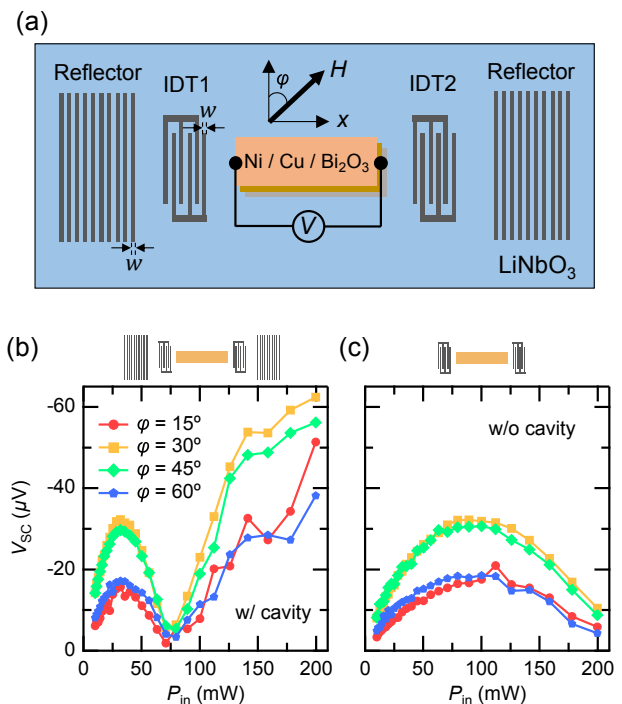


Fig. 1. (Color online) (a) A Schematic illustration of the acoustic cavity device structure used for the spin current generation. Each IDT consists of 50 metallic stripes. Each set of resonator gratings consists of 200 metallic stripes. The width of metallic stripes of IDT and resonators w and the space between metallic stripes d are both set to 300 nm. SAWs propagate along the x -axis. External in-plane magnetic field H is applied with the in-plane angle ϕ as shown in the schematic. A Ni (10 nm)/Cu (20 nm)/Bi₂O₃ (20 nm) heterostructure was deposited between two IDTs. (b, c) Measured spin current signals at various in-plane magnetic field angles ϕ of the sample (b) with acoustic cavity and (c) without acoustic cavity.

layer.^{9,15–20)} The spin current flowing to the interface between Cu and Bi₂O₃, which forms a Rashba spin splitting interface,^{21,22)} is converted to charge current by the inverse Edelstein effect (IEE).^{9,15,16,23)}

3. Spin Pumping Voltage Measurement

SAWs are generated by applying a radiofrequency (RF)



power P_{in} to IDT1 while applying an external in-plane magnetic field H , as shown in Fig. 1(a). During the magnetic field sweep, electrical output voltage generated by the IEE can be detected. By symmetric Lorentzian fittings of the voltage signal, we estimated the generated voltage V_{SC} due to spin-to-charge conversion as described in our previous work.⁹⁾ Figures 1(b) and 1(c) show the measured V_{SC} versus P_{in} at various in-plane magnetic field angles φ to the perpendicular axis of the SAW propagation direction. We measure the signals of two devices; one with the acoustic cavity [Fig. 1(b)] and one without the acoustic cavity [Fig. 1(c)]. The SAW excitation frequency is $f_{\text{SAW}} = 3.035$ GHz. As shown in Fig. 1(b), in the presence of the acoustic cavity, V_{SC} shows a local maximum at $P_{\text{in}} \sim 30$ mW and starts to decrease at higher P_{in} . It shows very strong suppression at $P_{\text{in}} \sim 75$ mW and starts to increase at higher P_{in} . On the other hand, in the absence of the acoustic cavity, as shown in Fig. 1(c), V_{SC} shows a local maximum at $P_{\text{in}} \sim 90$ mW, which is 60 mW higher than the value in the presence of the acoustic cavity. Figures 1(b) and 1(c) also show that the tendency of V_{SC} does not vary with $\varphi = 15, 30, 45$, and 60° . These results indicate that the threshold power of the nonlinear regime of the spin current generation does not rely on φ . Since the amplitude of the generated spin current by spin pumping depends on the intensity of the excited FMR, and the FMR depends on φ ,^{9,13–16)} we concluded that this nonlinearity is not caused by nonlinearity of magnetic dynamics. It indicates that the nonlinearity is probably transferred from SAWs in contrast to other experiments about nonlinearities of SAW-driven quasiparticles.^{24,25)} Therefore, we focus on the nonlinear behavior of phonons, which in principle, does not depend on φ .

4. SAW Transmission at Various Input Power

To clarify the origin of the nonlinear behavior of V_{SC} , we measured SAW transmission without applying an external magnetic field, thus we detect signals only from phonons. We excite SAWs by applying P_{in} to IDT1 and we detect propagated SAWs in IDT2 as an electric signal P_{out} . We fix the amplitude of P_{in} and sweep the frequency f , we measure P_{out} at f . First, we measure P_{out} of the sample without any deposited materials between the two IDTs, which we refer to as “the sample without a ferromagnetic layer (without FM)” hereafter, at various P_{in} values, as shown in Figs. 2(a) and 2(b). We also measure P_{out} of the sample with a Ni/Cu/Bi₂O₃ heterostructure, which we refer to as the sample with a ferromagnetic layer (with FM) hereafter, at various P_{in} values, as shown in Figs. 2(c) and 2(d). We note that all the measurements in Fig. 2 are done in the presence of the acoustic cavity.

The SAW transmission signals have two significant groups of peaks. The first group is detected from the low P_{in} range. And the second group is detected only in $P_{\text{in}} \geq 30$ mW. The peaks are almost equally separated. The appearance of equally separated peaks agrees with a behavior previously reported in other cavity studies.^{26,27)} A detailed interpretation of the equally separated peaks can be found in Supplemental Materials.²⁸⁾ The second group of peaks at a higher frequency regime arises from the equally separated peaks. However, it is not detectable at low P_{in} since it is far from the effective detection range centered around the main resonance fre-

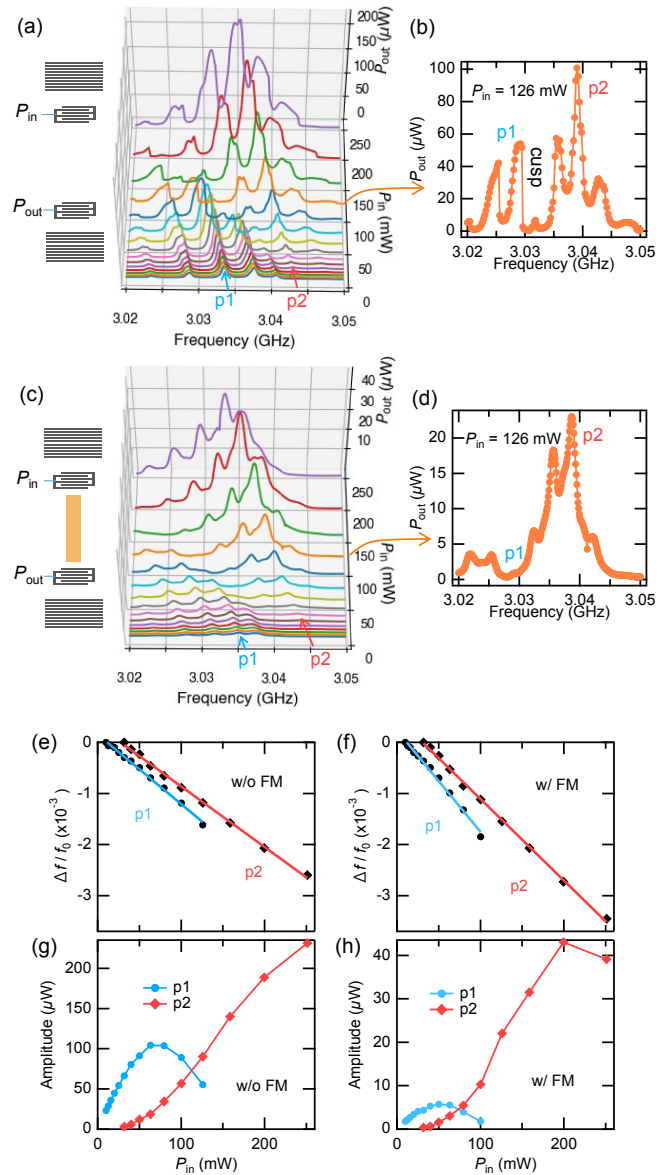


Fig. 2. (Color online) (a) SAW transmission signals P_{out} of the sample with the acoustic cavity in the absence of any deposited materials between two IDTs (w/o FM) in a frequency domain at various input powers to the IDT1, P_{in} , and (b) when $P_{\text{in}} = 126$ mW. (c) SAW transmission signals P_{out} of the sample with the acoustic cavity including Ni/Cu/Bi₂O₃ layers between two IDTs (w/FM) in a frequency domain at various input powers to the IDT1, P_{in} , and (d) when $P_{\text{in}} = 126$ mW. No external magnetic field (i.e., $H = 0$) is applied for (a)–(d). There are two groups of peaks and we set two significant peaks as p1 and p2, as pointed out in (a)–(d). (e, f) Frequency shifts $\Delta f/f_0$ of p1 and p2 versus P_{in} of the acoustic cavity samples. We set f_0 as the value at $P_{\text{in}} = 10$ mW for p1 and 32 mW for p2. Solid lines exhibit linear fittings. (g, h) Amplitudes of p1 and p2 versus P_{in} of the acoustic cavity samples. We estimated resonant frequencies and amplitudes of p1 and p2 in (e)–(h) by Gaussian fittings.

quency. Conversely, when $P_{\text{in}} \geq 30$ mW, the second group comes near the effective detection range due to a frequency shift that will be discussed below. In the following, we will extract information from two representative peaks, one from each of these groups, that we will label p1 and p2, as pointed out in Figs. 2(a)–2(d). We calculate the Q-factor which is typically used to estimate the quality of a cavity.^{27,29)} For the sample without FM, the maximum Q-factor is 2,960 for p1 and 6,749 for p2. For the sample with FM, the maximum Q-

Table I. The frequency shift coefficient k value of various samples.

| Sample | Peak | k (mW ⁻¹) |
|--------|------|-------------------------|
| w/ FM | p1 | -13.6 (0.3) |
| | p2 | -11.9 (0.2) |
| w/o FM | p1 | -19.6 (0.8) |
| | p2 | -16.7 (0.3) |

factor is $\sim 2,500$ for both p1 and p2. The detail of the estimation of Q-factors is shown in Supplemental Materials.²⁸⁾

The resonant frequency of peaks, f_{res} shifts when P_{in} increases. We define the frequency shift as $\Delta f/f_0$, where $\Delta f = f_{\text{res}} - f_0$ and f_0 is the resonant frequency at $P_{\text{in}} = 10$ mW. We estimate P_{in} dependence on the frequency shifts of p1 and p2 of the sample without FM in Fig. 2(e) and with FM in Fig. 2(f). The frequency shifts of p1 and p2 are well fitted with the following linear relation with P_{in} :

$$\Delta f/f_0 = kP_{\text{in}}. \quad (1)$$

Here, k denotes a phenomenological coefficient of the frequency shift. The coefficient k values of each peak and each sample are shown in Table I where the inside of the parenthesis exhibits errors of each value. We will further discuss these frequency shifts below. Also, we show P_{in} dependence of the amplitudes of p1 and p2 of the sample without FM in Fig. 2(g) and with FM in Fig. 2(h). The amplitude of p1 increases at the regime $P_{\text{in}} < 70$ mW and starts to decrease at $P_{\text{in}} \sim 70$ mW. As the amplitude of p1 starts to decrease, the slope of the amplitude of p2 becomes larger. We also performed the same measurements with the samples without the acoustic cavity. We detected similar frequency shifts to that of the samples with the acoustic cavity (see Supplemental Materials²⁸⁾), however, the appearance of higher frequency peaks at high P_{in} was not observed.

5. SAW Frequency Shift due to the Temperature

It is known that resonant frequencies of SAWs on a LiNbO₃ substrate shift depending on the temperature due to sound velocity variation.³⁰⁾ To clarify a temperature contribution to the frequency shifts of our samples, we measure temperatures using an infrared camera (optris PI 640i). We set areas A1, A2, and A3 shown in Fig. 3(a), and measure the mean temperatures of each area during applying an RF power P_{in} to IDT1. We apply two types of RF power to IDT1: a continuous wave (CW) which is equivalent to the RF power used in Fig. 2; and a pulse modulation of the CW that is expected to reduce Joule heat by giving the IDT time to cool down. The voltage signal of the CW and the pulse-modulated wave measured by an oscilloscope are shown in Figs. 3(b) and 3(c), respectively. The rate, period, and width of the pulse modulation are, respectively, 2.702 MHz, 370 ns, and 200 ns. Figures 3(d) and 3(e) show the measured temperatures at various P_{in} values. The results show that the temperatures of each area are linearly proportional to P_{in} , thus we can fit the power dependences of the temperatures as

$$T = T_0 + sP_{\text{in}}, \quad (2)$$

where T is the detected temperature, T_0 is the detected temperature when no RF power is applied ($P_{\text{in}} = 0$) under room temperature, and s is a linear coefficient constant. The fitting results of the input power dependence of the detected

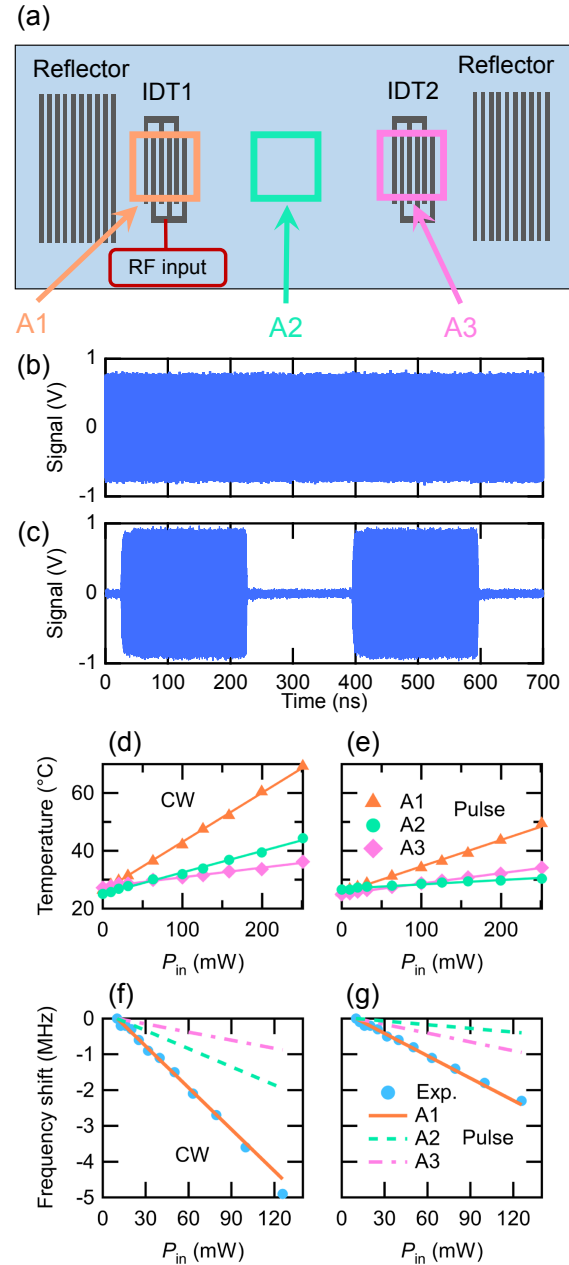


Fig. 3. (Color online) (a) A schematic illustration of thermal detection areas A1–A3 of the acoustic cavity device. (b, c) Voltage signal of (b) continuous wave and (c) pulse-modulated wave measured by an oscilloscope when the input power is 10 dBm. (d, e) Measured mean temperatures of A1 (triangle), A2 (circle), and A3 (diamond) when (d) the CWs and (e) pulse-modulated waves are applied to IDT1. Solid lines exhibit linear fittings using Eq. (1). (f, g) Frequency shifts of p1 (circles) when (f) the CWs and (g) pulse-modulated waves are applied. The orange solid lines exhibit the calculated frequency shift by temperature using the parameter and the linear constant contained in (d) and (e).

temperature are shown as solid lines in Figs. 3(d) and 3(e). The constant s values of the fittings in Figs. 3(d) and 3(e) are shown in Table II. As one can find from the values of s , applying pulsed waves reduces Joule heat. Now, we have the coefficients of the frequency shift in Table I and the coefficients of the temperature increase in Table II. Using these coefficients, and the phenomenological coefficient of the frequency shift by temperature difference given in Ref. 30; $\sigma = 7.5 \times 10^{-5} \text{ } ^\circ\text{C}^{-1}$, we can calculate the input power dependences of the frequency shifts as

Table II. The slope of linear fittings in Figs. 3(b) and 3(c).

| RF power | Area | Slope ($\times 10^{-3} \text{ }^\circ\text{C mW}^{-1}$) |
|----------|------|---|
| CW | A1 | 170.0 (2.2) |
| | A2 | 33.2 (1.2) |
| | A3 | 74.0 (1.7) |
| pulsed | A1 | 91.5 (2.2) |
| | A2 | 35.9 (0.5) |
| | A3 | 15.1 (1.1) |

$$\Delta f = \sigma f_0 \Delta T = \sigma s f_0 P_{\text{in}}, \quad (3)$$

where $\Delta T = T - T_0$. The calculated frequency shifts versus temperature increase of each area using Eq. (3) are shown as solid and dashed lines in Figs. 3(f) and 3(g). Real frequency shifts detected by the signal generator are also plotted with markers. The calculations using the mean temperature of A1 are in good agreement with the detected frequency shifts, indicating that $\sigma = k/s$. Therefore, we conclude that the frequency shifts of SAWs are caused by temperature increases originating from Joule heat.

As we mentioned before, the nonlinear behavior of spin current generation in the acoustic cavity device [Fig. 1(b)] is larger than in the device without the acoustic cavity [Fig. 1(c)]. Although IDTs act as a low-efficiency cavity adding acoustic Bragg reflectors increases the Q-factor of the cavity. Therefore, reducing the linewidth of the SAW modes inside the cavity as well as increasing their amplitudes. In addition, because p1 (p2) shifts out from (into) the reflection regime of the acoustic cavity, its amplitude becomes smaller (larger). By the calculation of the squared magnitude of the reflection coefficient ($|\Gamma|^2$) of Bragg reflectors, we show that a certain frequency range where Bragg reflection occurs near the Bragg frequency,²⁹ which implies the reflection regime of the acoustic cavity by coupling-of-modes theory^{29,31} in Supplemental Materials.²⁸ The frequency dependence of $|\Gamma|^2$ shows the maximum value (Bragg frequency) at 3.035 GHz, and the linewidth of $|\Gamma|^2$ is 14.7 MHz, which well supports this hypothesis. The other phenomenon for which an interpretation is missing is the shape change of the peaks. As shown in Fig. 2(a), when P_{in} is high (>120 mW), p1 is curved and has a cusp, and the P_{out} signal starts to decrease immediately at a higher frequency. This curved shape observed at high power exhibits a resemblance to nonlinear oscillations, such as the Duffing oscillation³² or the quantum mechanical model of a Kerr resonator.³³ This behavior is not present in Fig. 2(c); specifically, it is only noticeable in the sample without FM, which has a larger Q-factor. Furthermore, the curved peaks cannot be observed in the device lacking Bragg reflector gratings (see Supplemental Materials²⁸).

Lastly, we show that these nonlinear behaviors can be projected to magnetic excitations and the nonlinear spin current generation in Figs. 1(b) and 1(c) can be explained by it. We measured the voltage signal as Figs. 1(b) and 1(c), but varied the frequency of P_{in} , as shown in Fig. 4. We subtract an average voltage at off-resonant field $\mu_0 H = 100\text{--}150$ mT from the voltage signal V and notate it as ΔV to eliminate background signals caused by SAWs.^{34–36} The voltage signal shows the separated groups of peaks and all the peaks shift when P_{in} increases, similar to the SAW peaks in Fig. 2(b). Especially, as one can find from the voltage peak

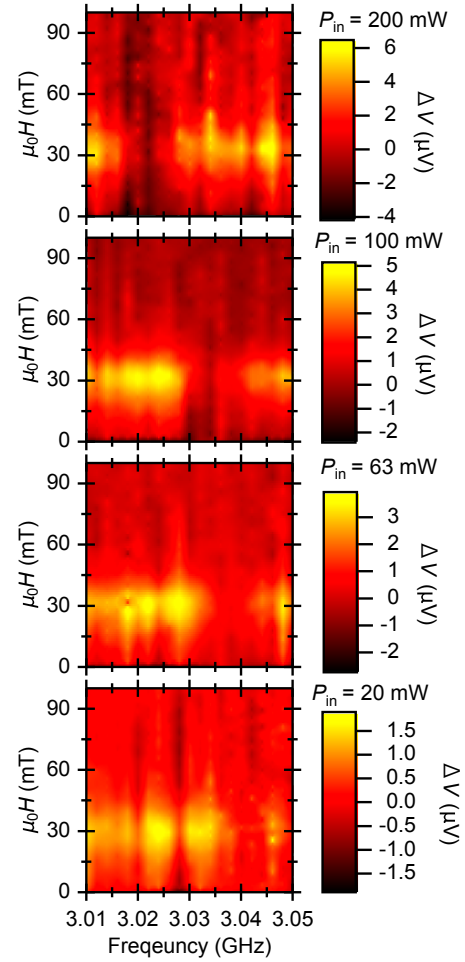


Fig. 4. (Color online) Measured voltage signals when various frequencies of P_{in} are applied under an external magnetic field H with an in-plane angle $\varphi = 45^\circ$. Each contour plot shows the voltage signal when the amplitude of P_{in} is as indicated. Voltage signals at each frequency are normalized by the average value at $\mu_0 H = 100\text{--}150$ mT to eliminate the background signal.

at the frequency of $f_0 = 3.034$ GHz when $P_{\text{in}} = 20$ mW in Fig. 4, the voltage signal shows a clear spin pumping signal. However, when P_{in} increases to 63 mW, no significant voltage signal exists at f_0 since the frequency shifts, underpinning the dip in Fig. 1(b). Thereafter, when P_{in} increases further, the voltage signal caused by p2 shifts and approaches f_0 . This voltage signal caused by p2 can explain the increase of the spin current signal at $P_{\text{in}} > 75$ mW in Fig. 1(b). Therefore, we confirm that the nonlinear behavior of SAWs due to Joule heating can be projected to magnetic excitations.

6. Conclusion

In summary, we detected frequency shifts, the appearance of a group of new peaks, and the peak shape change of SAWs when the applied RF power to an IDT increased. We clarified that the frequency shift of SAWs is caused by Joule heating, and it can be detected whether the device has an acoustic cavity or not. However, changes in the peak shape and the appearance of peaks at higher frequencies and high input power are only detectable when the device includes an acoustic cavity and does not originate from Joule heating. Therefore, a higher-quality cavity can induce the observed nonlinear behavior. We demonstrated that the nonlinear

behavior of SAWs can be projected to magnetic excitations by magnon–phonon coupling. Owing to the increased interest in spintronic studies with SAWs,³⁷⁾ our findings can provide useful information for fundamental and industrial research.

Acknowledgment Y.H. wishes to thank RIKEN Junior Research Associate Program for supporting this work. This work was partially supported by Grants-in-Aid for Scientific Research (S) (No. 19H05629) and the Japan Society for the Promotion of Science Grants-in-Aid for Scientific Research (No. 20H01865).

*jorgeluis.pueblanunez@riken.jp

†yotani@issp.u-tokyo.ac.jp

- 1) L. D. Landau and E. M. Lifshitz, *Mechanics* (Butterworth-Heinemann, New York, 1976) 3rd ed.
- 2) R. Lifshitz and M. C. Cross, *Nonlinear Dynamics of Nanomechanical and Micromechanical Resonators* (Wiley, New York, 2008).
- 3) S. M. Hendrickson, A. C. Foster, R. M. Camacho, and B. D. Clader, *J. Opt. Soc. Am. B* **31**, 3193 (2014).
- 4) E. Okamoto, *Nonlinear Theory Its Appl.*, *IEICE* **12**, 257 (2021).
- 5) M. Planat, D. Hauden, J. Gros Lambert, and J. J. Gagnepain, *IEEE Int. Freq. Cont.*, **1980**, p. 255.
- 6) X. Pang and Y. K. Yong, *IEEE Trans. Ultrason. Ferroelectr. Freq. Control* **67**, 422 (2020).
- 7) L. Shao, N. Sinclair, J. Leatham, Y. Hu, M. Yu, T. Turpin, D. Crowe, and M. Lončar, *Opt. Express* **28**, 23728 (2020).
- 8) L. Shao, W. Mao, S. Maity, N. Sinclair, Y. Hu, L. Yang, and M. Lončar, *Nat. Electron.* **3**, 267 (2020).
- 9) Y. Hwang, J. Puebla, M. Xu, A. Lagarrigue, K. Kondou, and Y. Otani, *Appl. Phys. Lett.* **116**, 252404 (2020).
- 10) D. L. T. Bell and R. C. M. Li, *Proc. IEEE* **64**, 711 (1976).
- 11) I. A. Feng, M. Tachiki, C. Krischer, and M. Levy, *J. Appl. Phys.* **53**, 177 (1982).
- 12) C. Caliendo and M. Hamidullah, *J. Phys. D* **52**, 153001 (2019).
- 13) M. Weiler, L. Dreher, C. Heeg, H. Huebl, R. Gross, M. S. Brandt, and S. T. B. Goennenwein, *Phys. Rev. Lett.* **106**, 117601 (2011).
- 14) L. Dreher, M. Weiler, M. Pernpeintner, H. Huebl, R. Gross, M. S. Brandt, and S. T. B. Goennenwein, *Phys. Rev. B* **86**, 134415 (2012).
- 15) M. Xu, J. Puebla, F. Auvray, B. Rana, K. Kondou, and Y. Otani, *Phys. Rev. B* **97**, 180301(R) (2018).
- 16) J. Puebla, M. Xu, B. Rana, K. Yamamoto, S. Maekawa, and Y. Otani, *J. Phys. D* **53**, 264002 (2020).
- 17) Y. Tserkovnyak, A. Brataas, and G. E. W. Bauer, *Phys. Rev. B* **66**, 224403 (2002).
- 18) K. Uchida, H. Adachi, T. An, T. Ota, M. Toda, B. Hillebrands, S. Maekawa, and E. Saitoh, *Nat. Mater.* **10**, 737 (2011).
- 19) K. Uchida, H. Adachi, T. An, H. Nakayama, M. Toda, B. Hillebrands, S. Maekawa, and E. Saitoh, *J. Appl. Phys.* **111**, 053903 (2012).
- 20) M. Weiler, H. Huebl, F. S. Goerg, F. D. Czeschka, R. Gross, and S. T. B. Goennenwein, *Phys. Rev. Lett.* **108**, 176601 (2012).
- 21) S. Karube, K. Kondou, and Y. C. Otani, *Appl. Phys. Express* **9**, 033001 (2016).
- 22) H. Tsai, S. Karube, K. Kondou, N. Yamaguchi, F. Ishii, and Y. Otani, *Sci. Rep.* **8**, 5564 (2018).
- 23) J. C. R. Sánchez, L. Vila, G. Desfonds, S. Gambarelli, J. P. Attané, J. M. de Teresa, C. Magén, and A. Fert, *Nat. Commun.* **4**, 2944 (2013).
- 24) M. V. Gustafsson, T. Aref, A. F. Kockum, M. K. Ekström, G. Johansson, and P. Delsing, *Science* **346**, 207 (2014).
- 25) R. Manenti, A. F. Kockum, A. Patterson, T. Behrle, J. Rahamim, G. Tancredi, F. Nori, and P. J. Leek, *Nat. Commun.* **8**, 975 (2017).
- 26) P. Kharel, G. I. Harris, E. A. Kittlaus, W. H. Renninger, N. T. Otterstrom, J. G. E. Harris, and P. T. Rakich, *Sci. Adv.* **5**, eaav0582 (2019).
- 27) D. Hatanaka, M. Asano, H. Okamoto, Y. Kunihashi, H. Sanada, and H. Yamaguchi, *Phys. Rev. Appl.* **17**, 034024 (2022).
- 28) (Supplemental Material) A description of equally separated frequency peaks in a cavity (S1) and information on the estimation of Q-factor (S2), SAW transmission at various input power of the sample without reflectors (S3), and reflection coefficient simulation (S4) are provided online.
- 29) K.-Y. Hashimoto, *Surface Acoustic Wave Devices in Telecommunications* (Springer, Berlin, 2000) p. 125.
- 30) S. Wu, Y. C. Chen, and Y. S. Chang, *Jpn. J. Appl. Phys.* **41**, 4605 (2002).
- 31) P. M. Smith, *Proceedings of 1995 SBMO/IEEE MTT-S International Microwave and Optoelectronics Conference, 1995*, Vol. 1, p. 265.
- 32) W. Wawrzynski, *Sci. Rep.* **11**, 2889 (2021).
- 33) N. Bartolo, F. Minganti, W. Casteels, and C. Ciuti, *Phys. Rev. A* **94**, 033841 (2016).
- 34) G. Weinreich and H. G. White, *Phys. Rev.* **106**, 1104 (1957).
- 35) T. Kawada, M. Kawaguchi, and M. Hayashi, *Phys. Rev. B* **99**, 184435 (2019).
- 36) T. Kawada, M. Kawaguchi, T. Funato, H. Kohno, and M. Hayashi, *Sci. Adv.* **7**, eabd9697 (2021).
- 37) J. Puebla, Y. Hwang, S. Maekawa, and Y. Otani, *Appl. Phys. Lett.* **120**, 220502 (2022).